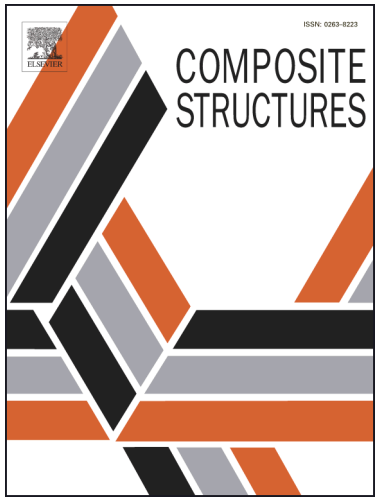

Aeroelastic assessment of cracked composite plate by means of fully coupled Finite Element and Doublet Lattice Method

Nur Azam Abdullah, Jose Luis Curiel-Sosa, Mahesa Akbar

PII: S0263-8223(17)33266-X
DOI: https://doi.org/10.1016/j.compstruct.2018.01.015
Reference: COST 9255

To appear in: *Composite Structures*

Please cite this article as: Abdullah, N.A., Curiel-Sosa, J.L., Akbar, M., Aeroelastic assessment of cracked composite plate by means of fully coupled Finite Element and Doublet Lattice Method, *Composite Structures* (2018), doi: https://doi.org/10.1016/j.compstruct.2018.01.015

Aeroelastic assessment of cracked composite plate by means of fully coupled Finite Element and Doublet Lattice Method

Nur Azam Abdullah[a,b,c,*], Jose Luis Curiel-Sosa[a,b], Mahesa Akbar[a,b]

[a] *Department of Mechanical Engineering, The University of Sheffield, The Portobello Centre, Sheffield, S1 4ET, United Kingdom*
[b] *Computer-Aided Aerospace and Mechanical Engineering Research Group (CA2M), University of Sheffield, Sheffield, United Kingdom*
[c] *Department of Mechanical Engineering, International Islamic University Malaysia, Malaysia*

Abstract

This paper presents an investigation on flutter speed of cracked composite plates. This work is divided into two sections: (a) variation of crack length at a fixed location on the plate, and (b) variation of crack location on the plate with a fixed crack length, modelled as a unidirectional composite for 0^0, 90^0 and 135^0 orientations. Mori-Tanaka homogenization model is applied to obtain the effective composite constitutive properties as the function of fiber and matrix volume fraction. Doublet Lattice Method (DLM) is used to calculate the unsteady aerodynamic forces, i.e., lift distributions. It is found that the existence of small crack ratio on the composite plate (less than 0.4) has triggered an increment of the flutter speed. To support this statement, flutter response modes for each crack ratio are plotted, where the structure appears to be more stiffened than the undamaged plate. However, the crack results in the reduction of flutter speed when the crack ratio reaches 0.5. For the crack location assessment, the flutter speed increases as the crack location moves from the root to the tip due to the reduction of flutter frequency. The results show a good agreement with the validation using Strip Theory considering unsteady aerodynamics.

Keywords: Flutter; Crack; Composite; Mori-Tanaka; Doublet Lattice Method, FEM.

1. Introduction

In this paper, computational investigations of the flutter effect to several cracked composite plates are performed. It is believed that the existence of crack will affect the stiffness of the structure [1]. There is a work that investigates the stiffness effect on symmetric laminates with arbitrary sequence [2]. The reduction in transverse and shear stiffness of the laminate as a function of the crack density in one ply was estimated by deriving an analytical solution. Thus, the accuracy in predicting the stress redistribution, from a cracked ply to the rest of the laminate has been achieved. Hence, it is a logical reason to investigate the flutter speed of cracked composite structures since one of the parameters that could affect the flutter speed estimation is the stiffness system.

Flutter is an instability problem due to structural vibration exerted by the aerodynamic load. Flutter often categorised as a self-excitation phenomenon, as the aerodynamic load is a function of the structural dynamic responses. A critical speed in which the structural vibration could lead to a catastrophic failure is called 'critical flutter speed'. One of the most well-known examples of flutter vibration leading to a catastrophic failure is well presented in the incident of the Tacoma bridge collapse on the 7^{th} of November 1940 [3].

It was reported that 42 mph speed of wind had excited several vibration modes on that day [4]. The dominant mode was moving vertically with a node at midspan and thus changed to torsional motion with a node at midspan abruptly. Within 4 seconds, the vibration amplitude has twisted the bridge about 45^0 before it collapse.

The existence of crack will affect the stiffness dis-

*Corresponding author
Email addresses: nababdullah1@sheffield.ac.uk (Nur Azam Abdullah), j.curiel-sosa@sheffield.ac.uk (Jose Luis Curiel-Sosa)
URL: http://www.jlcurielsosa.org (Jose Luis Curiel-Sosa)

tributions as discussed in the literature. It is also a requirement to determine the flutter boundary by considering the structural stiffness. Castravete and Ibrahim demonstrated that the stiffness significantly affects the flutter boundary [5]. This evidence has attracted attention to investigating the flutter boundary when there is an existence of crack on the structure.

In studying the circumstance, one of the aircraft crash incidents of North American P-51D Mustang that related to the event is referred as an example. The racing aircraft which also known as "The Galloping Ghost" crashed at the National Championship Air Races in Reno/Stead Airport, Nevada, USA. The technical investigation report by National Transportation Safety Board (NTSB) revealed that the existing fatigue crack in one screw caused the reduction of elevator trim tab stiffness [6]. This situation had triggered aerodynamics flutter to occur at racing speed.

There are some works reported regarding supersonic flutter on damaged composite such that shear deformable laminated composite flat panels by Birman and Librescu [7], microstructural continuum damage by Pidaparti [8] and, Pidaparti and Chang [9]. The coupling between two-dimensional static aerodynamic technique and a higher order transverse shear deformation theory for the structural plate model were performed in [7]. Aerodynamic models of Piston theory were applied, and the structures were modelled based on the damage mechanics theory with an internal state variable to mark damage characteristic in the material [8], [9].

There is a work that model a crack on a composite panel using XFEM at the supersonic region presented in [10]. A rectangular plate made of a Functionally Graded Material (FGM) is considered in this work as an advanced composite structure. The recent investigation of interaction between cracks on flutter was presented by Viola et al. [11]. The numerical flutter analysis was performed on a multi-cracked Euler-Bernoulli beams under subtangential force as the non-conservative dynamic load.

Some researchers applied the probabilistic approach to assess the flutter failure of a composite structure with crack in subsonic flow. The application of Monte Carlo simulation in [12] and Polynomial Chaos Expansion method in [13] show the statistical studies of flutter with the presence of multiple damage uncertainties.

Based on the overview, it can be seen that there is a lack of publication on the flutter of cracked composite. Moreover, at subsonic regime, to the authors knowledge, only Wang et al. [14] studied it by means of analytical/semi-computational model. As most transport and light aircrafts are operating in subsonic regime, thus it is considered a great benefit to investigate the flutter effect on cracked composite within this airspeed regime.

In the present work, a novel implementation of fully computational approach to investigate the flutter on cracked composite within subsonic regime is elaborated. Laminated finite element is used to model the composite structure. The load is modelled as unsteady aerodynamic load in frequency domain by means of Doublet Lattice Method (DLM). The pk-method is applied to obtain the flutter solution. In the following sections, the general overview of the computational methods used are presented.

2. Flutter speed determination

Flutter is defined as a state or phenomenon of flight instability which can cause structural failure due to the unfavourable interaction of aerodynamics, elastic, and inertia forces [15]. Flutter can deform an aircraft due to dynamics instability. In practice, structural damping, g versus velocity, V for each mode shape is plotted to determine the flutter speed graphically. Based on the Federal Aviation Administration Regulations in [16], the required structural damping, (g) value for plotting Fig. 1 must exceed more than 3%, $g > +0.03$ in the unstable region so that the plot can be stated as in flutter region.

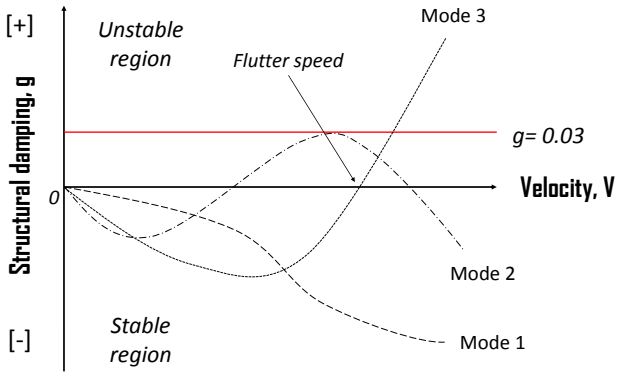

Figure 1: Structural damping graph guided by FAA (2004)

The procedure has been performed by Nissim and Gilyard [17] to estimate the flutter speed experimen-

tally by using the parameter identification technique. It is pointed out that there is an issue of difficulty when the 'exact' analytical scheme to solve the flutter equations. Since the damping merged with aerodynamic terms only, the system is assumed to be an undamped structural system. This is the reason why the system excitation at zero damping that led to the zero dynamic pressure could not be performed and hence will trigger the responses at resonance become infinite values. To solve this, the 3% of structural damping is assumed and at the same time, the responses of the 'exact system' is calculated. When this procedure objective is achieved, the flutter speed can be determined at zero structural damping.

Fig. 1 is referred as an explanation for the flutter phenomenon in graphical presentation. Mode 1 moves towards the instability region in the first place, but the plot free from the unstable region as the speed is increasing. Mode 2 crosses the velocity axis where the structural damping is zero. Since the plot of Mode 2 still has not exceeded $g = 0.03$, the structure is in a safe zone. Mode 3 crosses the velocity axis where the structural damping is zero and has surpassed the limitation of $g = 0.03$. It is concluded that Mode 3 is the most dangerous state where the flutter is expected to happen.

In this study, the flutter speed for each composite structure is determined by using this technique. Several parameters are concerned to be investigated; the unidirectional composite angle, θ, crack ratio, η and the dimensionless crack location, ξ_c.

3. Mean field homogenization

In this part, a process called homogenization which is considered to represent the composite material properties is performed. Representative volume element (RVE) is used to represent the microscale of the structure. Solving the mesoscale iteration at every guess, the RVE is computed, and then, the information is passed to macroscale. The homogenization procedures are explained more in [18],[19] and [20].

The objective of applying this process is to estimate the stresses and strains as the matrix and the fibers are mixed. In this study, the homogenization of composite structures is carried out by applying the Eshelby method. Fig. 2 shows the schematic diagram of homogenization based on the Eshelby method presented in [21] and [22].

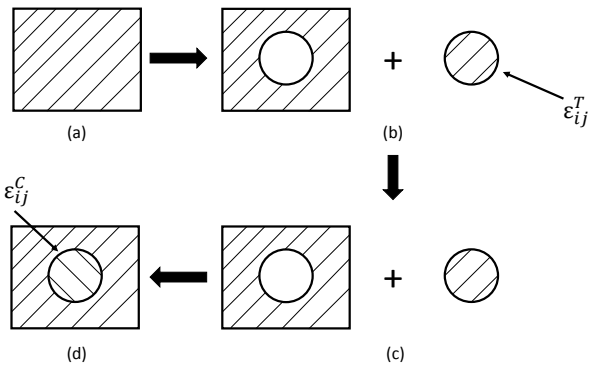

Figure 2: Schematic diagram of homogenization based on the Eshelby method

Fig. 2 (a) shows an initial unstressed elastic homogeneous material. A visualization of a cutting section called as inclusion is assumed to this structure, presented as the circle. The inclusion is presumed encounters a shape change free behaviour; causing the transformation strain $\boldsymbol{\varepsilon}_{ij}^T$ in Fig. 2 (b) from the constraining matrix.

Assuming the strain is uniform within the inclusion, the stress in the inclusion, $\boldsymbol{\sigma}_{ij}^I$ is estimated using Eq. 1.

$$\boldsymbol{\sigma}_{ij}^I = \boldsymbol{C}_{ijkl}^M(\boldsymbol{\varepsilon}_{kl}^C - \boldsymbol{\varepsilon}_{kl}^T) \tag{1}$$

The constraining strain can be determined in the form of transformation strain, ε_{kl}^T as shown in Eq. 2.

$$\boldsymbol{\varepsilon}_{ij}^C = \boldsymbol{S}_{ijkl}\boldsymbol{\varepsilon}_{kl}^T \tag{2}$$

The Eq. 2 is substituted in Eq. 1 to compute the stress in the inclusion. The equation is simplified in Eq. 3.

$$\boldsymbol{\sigma}_{ij}^I = \boldsymbol{C}_{ijkl}^M(\boldsymbol{S}_{klmn} - \boldsymbol{I}_{klmn})\boldsymbol{\varepsilon}_{mn}^T \tag{3}$$

The 4-th rank identity tensor of $\boldsymbol{I}_{klmn}$ in Eq. 3 is given in Eq. 4.

$$\boldsymbol{I}_{klmn} = \frac{1}{2}(\delta_{km}\delta_{ln} + \delta_{kn}\delta_{lm}) \tag{4}$$

Eq. 3 is transformed in vector and matrices form as in Eq. 5, where the braces and brackets are indication of vector and matrices, respectively.

$$\boldsymbol{\sigma}^I = \boldsymbol{C}^M(\boldsymbol{S} - \boldsymbol{I})\boldsymbol{\varepsilon}^T \tag{5}$$

As the fiber is assumed as infinite long cylindrical, the expressions of Eshelby tensors are estimated in form of matrix Poisson's ratio as in Eq. 6 to Eq. 14.

$$S_{1111} = S_{2222} = \frac{5 - \upsilon_m}{8(1 - \upsilon_m)} \tag{6}$$

$$S_{3333} = 0 \tag{7}$$

$$S_{1122} = S_{2211} = \frac{-1 + 4\upsilon_m}{8(1 - \upsilon_m)} \tag{8}$$

$$S_{1133} = S_{2233} = \frac{\upsilon_m}{2(1 - \upsilon_m)} \tag{9}$$

$$S_{3311} = S_{3322} = 0 \tag{10}$$

$$S_{1212} = S_{1221} = S_{2112} = S_{2121} = \frac{3 - 4\upsilon_m}{8(1 - \upsilon_m)} \tag{11}$$

$$S_{1313} = S_{1331} = S_{3113} = S_{3131} = \frac{1}{4} \tag{12}$$

$$S_{3232} = S_{3223} = S_{2332} = S_{2323} = \frac{1}{4} \tag{13}$$

Otherwise,

$$S_{ijkl} = 0 \tag{14}$$

Eshelby tensors of the inclusion as the function of matrix material properties and inclusion geometry or shape are applied. The assumption made in this case where the shape is an infinite long cylinder as shown in Eq. 15.

$$\boldsymbol{S}_{MnAb} = f(\boldsymbol{C}_m, l \to \infty) \tag{15}$$

In this study, the effective composite properties of the composite plates are obtained by using Mori-Tanaka method as shown in [23] and [24].

The effective material properties via Mori-Tanaka of composite $\boldsymbol{C}_{comp}$ is expressed in Eq. 16, where V, $\boldsymbol{C}$ and $\boldsymbol{A}^{MT}$ are the volume fraction, the material properties constitutive equation and the concentration tensor based on Mori-Tanaka method with respect to fiber, f and matrix, m, respectively.

$$\boldsymbol{C}_{comp} = V_m \boldsymbol{C}_m \boldsymbol{A}_m^{MT} + V_f \boldsymbol{C}_f \boldsymbol{A}_f^{MT} \tag{16}$$

The Mori-Tanaka tensor equation is shown in Eq. 17 where $\boldsymbol{A}^{di}$ is the dilute concentration tensor and $\boldsymbol{I}$ is the identity matrix. The dilute tensor equation is expressed in Eq. 18.

$$\boldsymbol{A}_f^{MT} = \boldsymbol{A}_f^{di}[V_m I + V_f \boldsymbol{A}_f^{di}] \tag{17}$$

$$\boldsymbol{A}_f^{di} = [\boldsymbol{I} + \boldsymbol{S}_{MnAb} \boldsymbol{C}_m^{-1} (\boldsymbol{C}_f - \boldsymbol{C}_m)]^{-1} \tag{18}$$

The properties are calculated as the function of fiber and matrix material properties, volume fractions and Eshelby tensors as summarised in Eq. 19.

$$\boldsymbol{C}_{comp} = f(\boldsymbol{C}_m, \boldsymbol{C}_f, V_m, V_f, \boldsymbol{S}_{MnAb}) \tag{19}$$

Fig. 3 shows the transformation of composite volume fraction to the homogenized composite using Mori-Tanaka method.

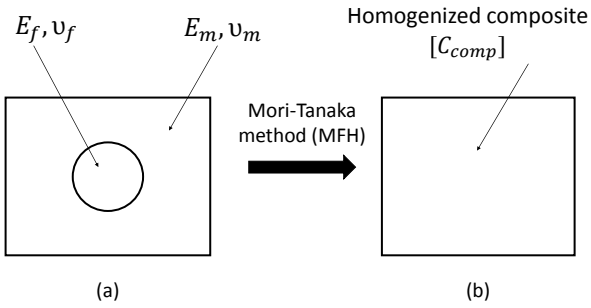

Figure 3: Mean field homogenization by Mori-Tanaka method

4. Aerostructural coupling

In this section, the Doublet Lattice Method (DLM) is used to predict the unsteady aerodynamics. Doublet Lattice Method has been developed by Albano and Rodden [25] to calculate the lift distributions in subsonic flow region.

The same coupling procedure between DLM and structural modelling using modified higher order shear deformation theory was performed by Abbas et al. [26] to estimate the flutter speed. There is another finite element that can be used, e.g. beam element, based on [27] but it is unattempted this time.

4.1. Finite element model

The 4-noded quadrilateral shell element is used in the finite element model. The boundary condition is fixed displacement on the root. The load used in the finite element model, is the aerodynamic load obtained via Doublet Lattice Method (DLM). This procedure allows for a coupling between the structure (finite element) and the aerodynamics (DLM).

The edge crack is modelled using double nodes in the chordwise direction. Two sets of nodes are assumed along the opposite face of the crack interface. The displacement fields of these two separated sets of nodes are independent to account the discontinuity along the crack interface.

4.2. Doublet lattice method

The specification of boxes along span and chord direction is required for coupling of FE-DLM using spline technique as shown in Fig. 4. To compute the unsteady aerodynamics modelling using DLM, a set number of elements called aerodynamics box is specified.

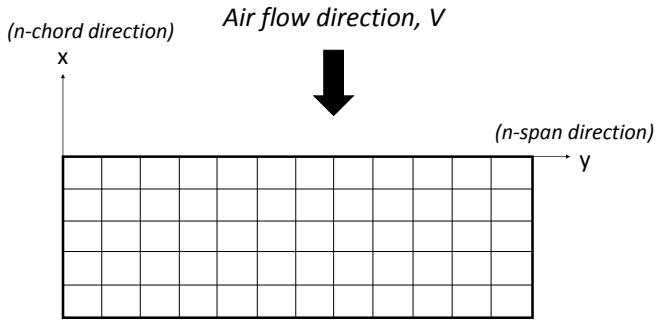

Figure 4: Aerodynamics modelling for coupling FE-DLM

The number of box, n and the constant force per unit length of the 1/4 chord line, f for each box is visualized. The strategy starts with the definition of doublet strength amplitude of the $j-th$ division as in Eq. 20; where l_j and $d\mu$ are the division line length and changes of length increment, respectively.

$$\frac{\bar{f}_j}{4\pi\rho}\int_{lj} d\mu \tag{20}$$

The normal wash amplitude generated at point (x_i,s_i), on the surface by $j-th$ number of doublet line is given in Eq. 21.

$$\bar{w}_j(x_i,s_i) = (\frac{\bar{f}_j}{4\pi\rho}U^2)\oint_{lj} K[x_i s_i; x_i(\mu), s_j(\mu)]d\mu \tag{21}$$

By summing the normal wash developed by $n-th$ doublet lines, the total normal wash at point $(x_i,\ s_i)$ is calculated. This relationship is presented in Eq. 22.

$$\bar{w}(x_i,s_i) = \sum_{j=1}^{n}(\frac{\bar{f}_j}{4\pi\rho}U^2)\oint_{lj} K[x_i s_i; x_j(\mu), s_j(\mu)]d\mu \tag{22}$$

$\bar{f}_j$ is evaluated by exerting Eq. 21 at n downwash points on the total surface of boxes. Eq. 23 is the pressure difference across the boxes surface; where the box area is calculated as $\Delta x_j cos\lambda_j$. The denotions of Δx_j and λ_j are the box average chord and doublet line sweep angle, respectively.

$$\bar{P}_j = \frac{\bar{f}_j}{\Delta x_j cos\lambda_j} \tag{23}$$

Thus, the new expression of parameters from Eq. 20 is shown in Eq. 24, considering the sweep angle of doublet line.

$$\frac{\bar{f}_j}{4\pi\rho}U^2 = \frac{1}{8}\pi\bar{p}_j\Delta x_j cos\lambda_j \tag{24}$$

Based on [25], the normal wash velocity can be estimated by implying the Kutta condition. The Kutta condition meets the requirement when each downwash point is the 3/4 chord point at a box midspan. By applying this specification, Eq. 21 is simplified in form of pressure distribution as expressed in Eq. 26.

$$\bar{w}_i = \sum_{j=1}^{n} D_{ij}\bar{p}_j \tag{25}$$

where,

$$D_{ij} = (\frac{1}{8}\pi)\Delta x_j cos\lambda_j \oint_{lj} K[x_i, s_i; x_j(\mu), s_j(\mu)]d\mu \tag{26}$$

In this study, the composite plate is considered as a thin plate where the panel is divided into several boxes for aerodynamics modelling. The thin composite panel is divided equally into 20 boxes in the spanwise direction and 5 boxes in the chordwise.

5. Flutter solution of *pk*-method

Here, the coupling of finite element model for structural and doublet lattice method for unsteady aerodynamics has been performed using spline technique. To estimate the flutter speed/ boundary in this study, the flutter solution based on pk-method shown in Eq. 27 is applied [28], where $\boldsymbol{M}_{hh}$ is the mass matrices,

$\boldsymbol{B}_{hh}$ is the damping matrices, $\boldsymbol{Q}_{hh}^{R}$ is the real aerodynamic matrices, $\boldsymbol{Q}_{hh}^{I}$ is the imaginary aerodynamic matrices and $\boldsymbol{K}_{hh}$ is the stiffness matrices.

$$\boldsymbol{M}_{hh}p^2 + (\boldsymbol{B}_{hh} - \frac{\frac{1}{4}\rho\bar{c}\boldsymbol{Q}_{hh}^{I}}{k})p + (\boldsymbol{K}_{hh} - \frac{1}{2}\rho V^2\boldsymbol{Q}_{hh}^{R}) = 0 \tag{27}$$

The term pk is referring to two parameters which are used to predict the flutter speed. p is the root of the quadratic equation and k is the reduced frequency in Eq. 27. To solve the reduced frequency of k, Eq. 28 is used where ω is the natural vibration mode frequency, $\bar{c}$ is the average chord length and V is the computed velocity.

$$k = \frac{\omega\bar{c}}{2V} \tag{28}$$

As the solution in Eq. 27 is in quadratic form of p, structural damping of g can be estimated as mentioned in Eq. 29.

$$p = \omega(2g + i) \tag{29}$$

To simplify the Eq. 28 and Eq. 29, the natural frequency that is obtained from modal analysis denoted by ω is eliminated. The relationship between g and V based on pk-method is now shown in Eq. 30.

$$p = \frac{2kV}{\bar{c}}(2g + i) \tag{30}$$

In the final solution of Eq. 30, this relationship is used to plot the structural damping, g versus airflow velocity, V to obtain the flutter speed. As mentioned in Section 2, the flutter speed is obtained at $g = 0$ where the structure begins to fail.

5.1. FE-DLM Coupling procedure

By using an interpolation technique, both structural and aerodynamic grids are associated. Thus, using this procedure allows the selection of both structural and aerodynamic of the lifting surfaces become independent to be performed in any particular theory of the fluid- structure interaction. An interpolation method called as 'splining' technique is used to interconnect both structural and aerodynamic model. The structure of the body can be modelled in one-, two- or three-dimensional array of grid points. For aerodynamic model, a lifting surface theory or strip theory might be used to model the aerodynamic boxes.

In this work, the composite plate is analysed with the existence of edge crack as shown in Fig. 5. Thus, it triggers the separation of the plate surface into subregions that has led to the discontinuous slope. For this reason, the aerodynamic degrees of freedom depends on the structural degrees of freedom. To make a relation between both models, a spline matrix is derived.

In general, the spline matrix that interpolates the displacements at the grid points of the structural finite element to the control points of aerodynamic boxes to resolve the data transferral problem. In Eq. 31, the total spline matrix of $\boldsymbol{G}_{kg}$ is expressed based on the generation of spline matrix by surface spline method, where u_k is the interpolated displacement vector at aerodynamic boxes, including the translational displacements and their slopes with respect to the components of the structural grid point deflections, u_g.

$$u_k = \boldsymbol{G}_{kg}u_g \tag{31}$$

Any grid components can be defined to describe the structural degrees of freedom. In this case, two transformations are required. The first one is the interpolation from the structural deflections to the aerodynamic deflections. The second one is the interpolation of the relationship between the aerodynamic loads and the structural equivalent loads acting on the structural grid point. From here, the aerodynamic degrees of freedom is correlated to be depending on the structural degrees of freedom. Further details about the aero-structure coupling of 'splining' technique can be explored in [29].

6. Cantilever unidirectional composite plate model

The unidirectional composite plate of graphite - fiber reinforced polyimide that is used in this study was developed in [30]. The unidirectional composite specimen model is presented in Fig. 5. It is modelled as a cantilever plate where the length, L is 0.5 m; the width, b is 0.1 m and the height, h is 0.005 m. As the crack development in this study is qualitatively measured, the crack ratio is defined as $\eta = a/b$ where a is the crack length. The dimensionless crack location for this study is denoted by $\xi_c = l/L$. The material properties of graphite - fiber reinforced polyimide is shown in Table 1.

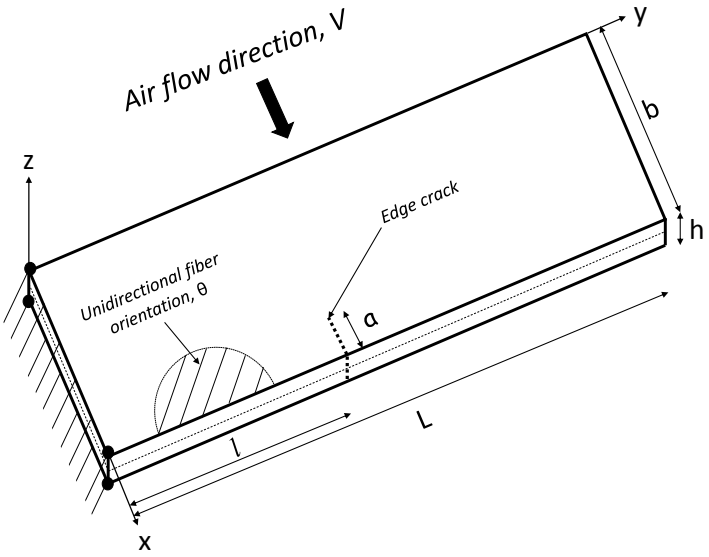

Figure 5: Specimen modelling of the unidirectional composite plate

Table 1: Material properties of graphite - fiber reinforced polyimide composite

Modulus of elasticity	$E_m = 2.76$ GPa	$E_f = 275.6$GPa
Poisson's ratio	$\nu_m = 0.33$	$\nu_f = 0.2$
Shear modulus	$G_m = 1.036$ GPa	$G_f = 114.8$ GPa
Mass density	$\rho_m = 1600\ kg/m^3$	$\rho_f = 1900\ kg/m^3$
Fiber volume fraction	$V = 0.5$	

6.1. Mean field homogenization (MFH) from Mori - Tanaka method

A code is developed to estimate the stiffness and the constitutive matrices based on Mori-Tanaka method for the presented composite structure. By using Chan-Unsworth model, the numerical properties calculated are compared with Mori-Tanaka method developed in this section. Figs. 6 and 7 present the stiffness matrices estimation of the material. Figs. 8 and 9 show the constitutive matrices estimation of the material.

As the Mori - Tanaka micromechanical model is implemented in this study, the constitutive equation in Plane Stress form $\boldsymbol{C}_{comp}$ [unit: Pa] is shown in Table 2:

6.2. Validation on vibration with modal analysis

Modal analysis is performed to validate the procedure used in this work. The benchmark results of vibration modes are compared with the results presented by Wang et al. [14]. In Table 3, the results of the modal analysis for a unidirectional composite of $\theta = 0$ using the presented method are shown and are compared with the results established in [14].

As the results of the modal analysis are validated, the procedure is applied to other specimens with existing crack. All eight vibrations modes (four bending modes and four torsion modes) that are presented in Table 3 are plotted in Fig 10.

It is a different modelling technique in observing the modal vibration modes. Thus, in this case, the finite element modelling has been applied to the unidirectional cracked composite panel instead of a cracked beam presented in [14]. In the reference, an analytical model was used to determine the natural frequencies/ mode shapes. Furthermore, a function of mode shapes was assumed to satisfy the boundary condition at the crack location. However, in the present paper, a full finite element model is used to obtain the mode shapes and the natural frequencies. Thus, for the plate with crack, the crack also modelled directly in the finite element model. Therefore, there will be discrepancies with the results compared to the reference. Further flutter analyses are presented in the next section.

Table 2: Constitutive values in plane stress form based on Mori-Tanaka method

$\boldsymbol{C}_{comp}$	Value (Pa)
$C_{11} = C_{22}$	6.8503 x10^3
$C_{12} = C_{21}$	3.1437 x10^3
$C_{13} = C_{23} = C_{31} = C_{32}$	0
C_{33}	2.646 x10^3

Table 3: First four bending modes and first four torsion modes vibrational frequencies for $\theta = 0^0$

Wang et al.	Mode	1st (Hz)	2nd (Hz)	3rd (Hz)	4th (Hz)
	Bending	6.94	43.47	121.71	238.49
	Torsion	62.81	197.45	329.08	460.71
Present work	Mode	1st (Hz)	2nd (Hz)	3rd (Hz)	4th (Hz)
	Bending	5.87	36.59	102.87	203.02
	Torsion	60.54	184.23	315.74	460.00
Relative error (Wang et al. and present work)	Mode	1st (Hz)	2nd (Hz)	3rd (Hz)	4th (Hz)
	Bending	15.35 %	15.83 %	15.48 %	14.87 %
	Torsion	3.61 %	6.69 %	4.05 %	0.15 %

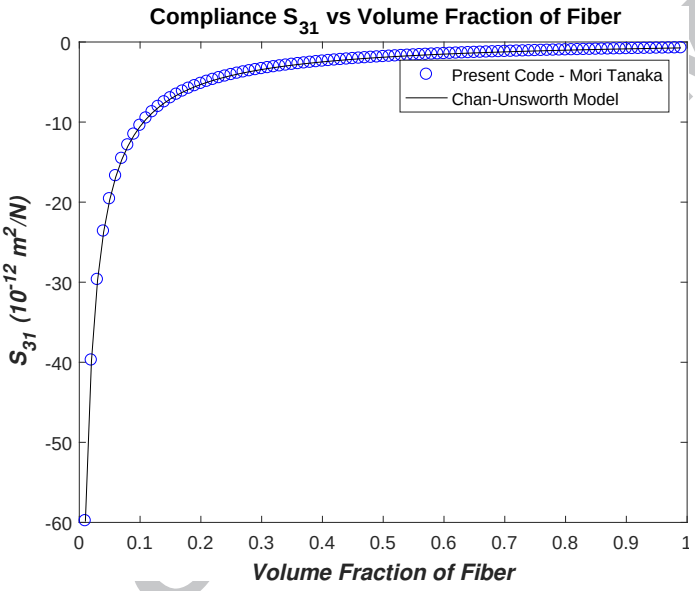

Figure 6: Effective stiffness matrix component of S_{31}

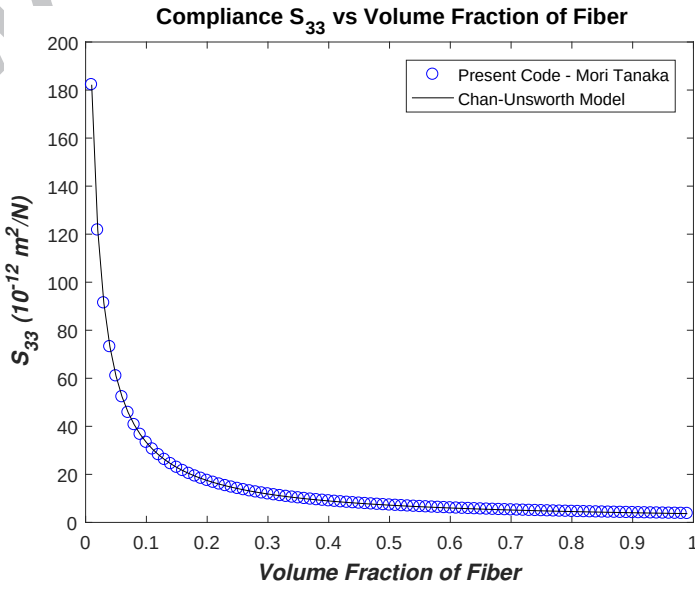

Figure 7: Effective stiffness matrix component of S_{33}

6.3. Section a: Flutter effects on the crack ratio

The objective of this subsection is to study the effects of the flutter speed while the crack location is fixed and the crack length is changed. Several analyses are performed to the unidirectional composites of 0^0, 90^0 and 135^0 orientations. The same procedures are repeated and applied for crack ratio denoted by $\eta = a/b$ as η is increased from 0 to 0.75.

The flutter analyses are performed to the undamaged (without crack) composite plates for 0^0, 90^0 and 135^0 orientations in the first place. The flutter speed for this situation is considered as the reference for other cases which is denoted as V_R. The flutter speed estimation for unidirectional composite without crack for 0^0, 90^0 and 135^0 orientations are shown in Fig. 11.

In this work, the frequency of vibrational mode interacting with the speed increment is presented in Fig. 12 for an oscillating composite plate at unidirectional of 0^0. Based on the plot, the flutter frequency is found to be 37.37 Hz, where the structural damp-

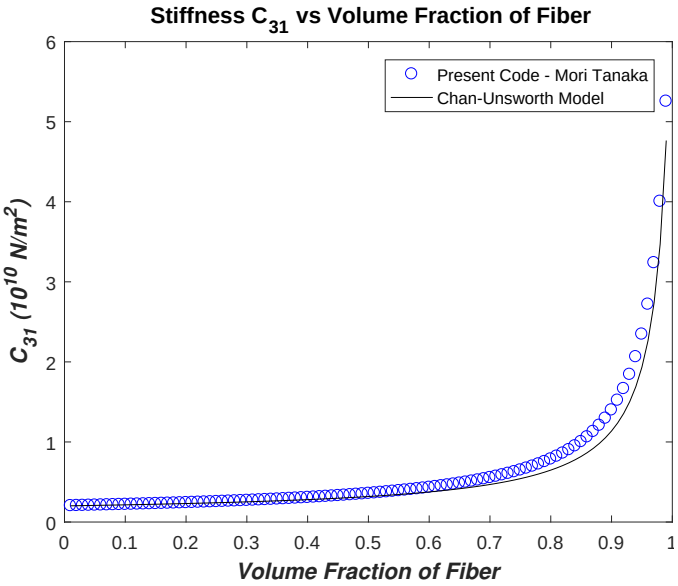

Figure 8: Effective stiffness matrix component of C_{31}

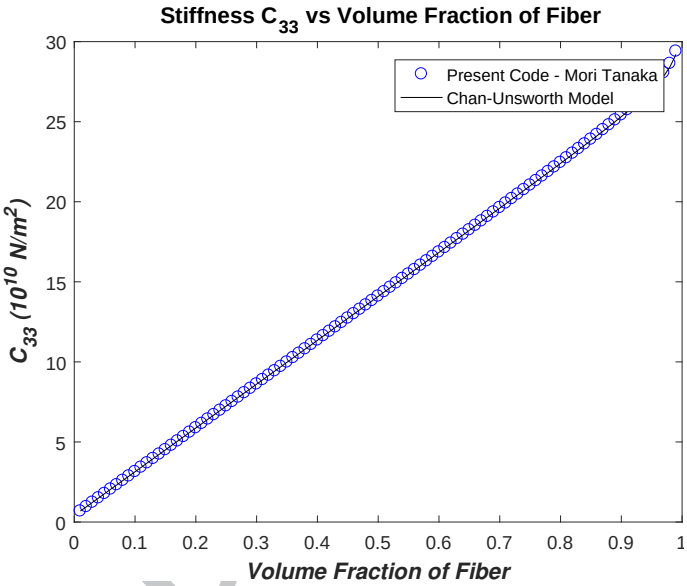

Figure 9: Effective stiffness matrix component of C_{33}

ing is zero. Using FEM-DLM approach, the flutter frequency for $\eta = 0.2$ is found to be a bit higher than the undamaged specimen.

As the flutter speeds of undamaged unidirectional composite plates at angle 0^0, 90^0 and 135^0 have been determined, the flutter analyses with crack planform are performed. The flutter speed, V_F is determined for several cases of crack ratio, $\eta = a/b$ which are 0.2, 0.25, 0.4, 0.5, 0.6 and 0.75. The normalized flutter speeds of V_F/V_R versus the crack ratio which are compared with results in [14] as shown in Fig. 13.

The results show that the flutter speeds are increasing for all presented composite angle when the crack ratio is 0.2 compared to the flutter speed of undamaged composite plates. The trends of flutter speed begin to decrease but are still above the reference flutter speed when $\eta = 0.25$. The same pattern is seen for crack ratio 0.4, but the flutter speed for this case is almost near to the flutter speed of the undamaged composite plate. At $\eta = 0.5$, the normalized flutter speeds of V_F/V_R for $\theta = 0^0$ and 90^0 begin to decrease about 1.84 % and 8.67 %, respectively. The same trend is found for $\theta = 135^0$ with $\eta = 0.5$ with a difference of 36.77%.

Based on these facts, the existence of crack ratio, η more than 0.4 makes the structure weaker from the undamaged plate ($\eta = 0$). As a result, the structure vibration amplitude tends to increase with the increment of crack ratio. This explanation shows an agreement with the work done by Song et al. [31] where the crack opening increment has weakened the cantilevered composite when it deals with dynamics loading. The results are almost similar to the results published in [14] where the flutter speed had found to be increased when the crack was initiated, but it began to decrease gradually when the η has reached 0.35. The same trend for present work is seen when the unsteady aerodynamics is modelled using strip theory as in Fig. 14.

To gain a deeper understanding of this phenomenon, flutter response modes are plotted in Fig. 15. This part aims to study the changes of the mode from without any crack until the specimen almost breaks where f_F is the flutter frequency for each case. In Fig. 15 (a) where $\eta = 0$, the flutter response mode is a first torsion mode, with $f_F = 37.37$ Hz. With the existence and increment of crack ratio, the flutter frequency keeps reducing, which allows more time for the structure to oscillate. Next, for $\eta = 0.2$ in Fig. 15 (b), the flutter response is the same mode as $\eta = 0.0$, with the deflection a little bit release. This behaviour made the structure be able to stand more load as the rigidity is now increased with the existence of small crack (0.02 m). Thus, it causes an increment of flutter speed compared to the undamaged specimen. The same behaviour of flutter response is seen until $\eta = 0.4$.

In Fig. 15 (e) where $\eta = 0.5$, the flutter speed is now reduced about 3.77 % compared to the undamaged specimen, but the flutter response mode is maintained. With further crack ratio increment, the flutter response mode has switched to the mixture

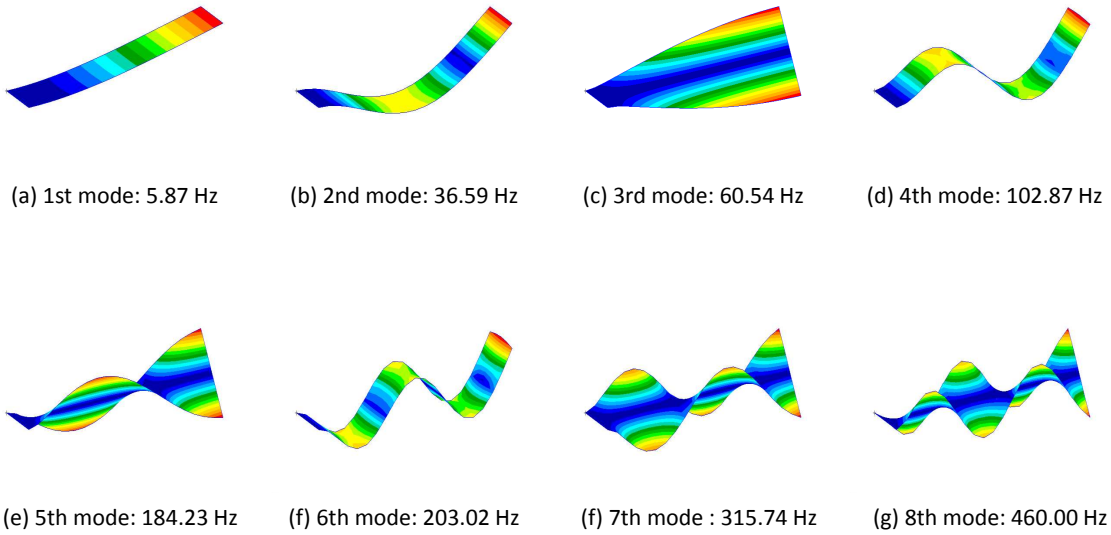

Figure 10: First eight vibration modes for $\theta = 0^0$

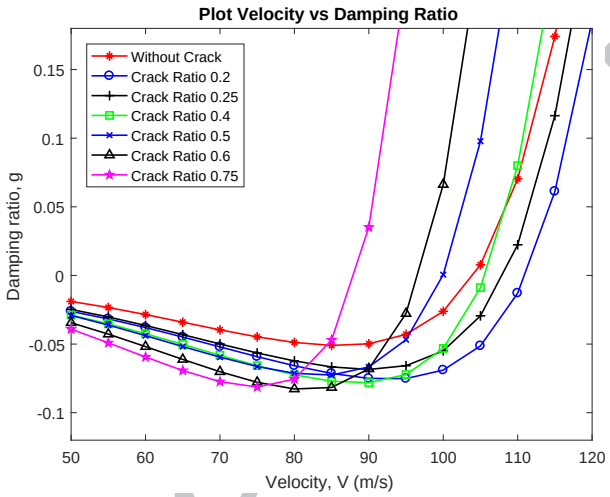

Figure 11: Flutter speed determination for $\theta = 0^0$

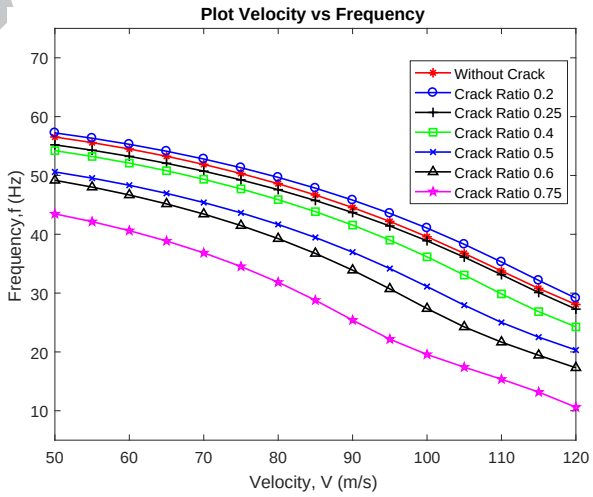

Figure 12: Flutter frequency reduction for $\theta = 0^0$

between torsion and bending mode as shown in Fig. 15 (g) for $\eta = 0.75$. For this case, the flutter speed has reduced to about 15.4 %.

6.3.1. Explanation on flutter speed increment for crack ratio of 0.2

DLM is applicable for interfering the lift distribution on flying surface in subsonic flow. It was developed based on the linearized aerodynamic potential theory. Thus, this method establishes a uniform undisturbed flow either in a steady flow or unsteady flow (with existence of gust) harmonically.

Aerodynamics modelling technique of DLM used in this work is much more advanced than Strip theory since it considers the structural panels, which allows the lifting surface to be divided into small trapezoidal lifting elements called as 'aerodynamic boxes'. As the lifting surfaces are assumed to be almost parallel to the freestream flow (refer Fig. 4), thus the arranged aerodynamic boxes also aligned in strip direction to be parallel to the airflow.

It is a different situation with strip theory modelling technique. The load at each spanwise station of a wing is assumed to be depending only on the motion of the station when flutter solution is computed. The lifting surface is divided into a set number of strips,

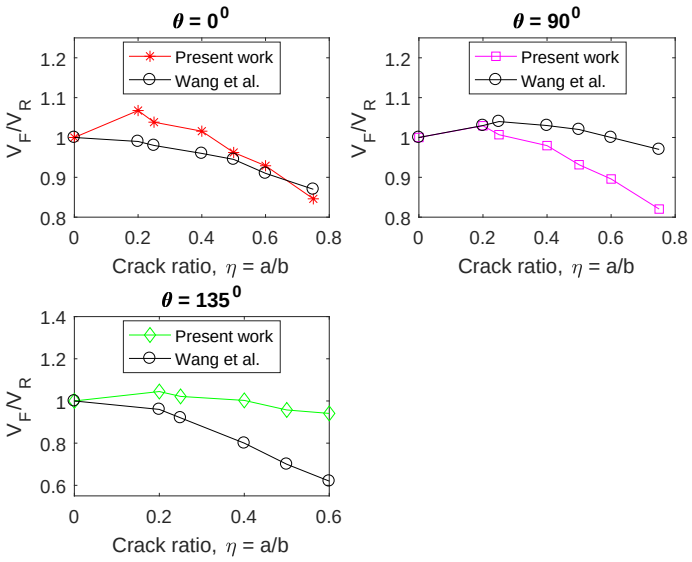

Figure 13: Normalized flutter speeds with respect to the crack ratio for case $\theta = 0^0$, $\theta = 90^0$ and $\theta = 135^0$

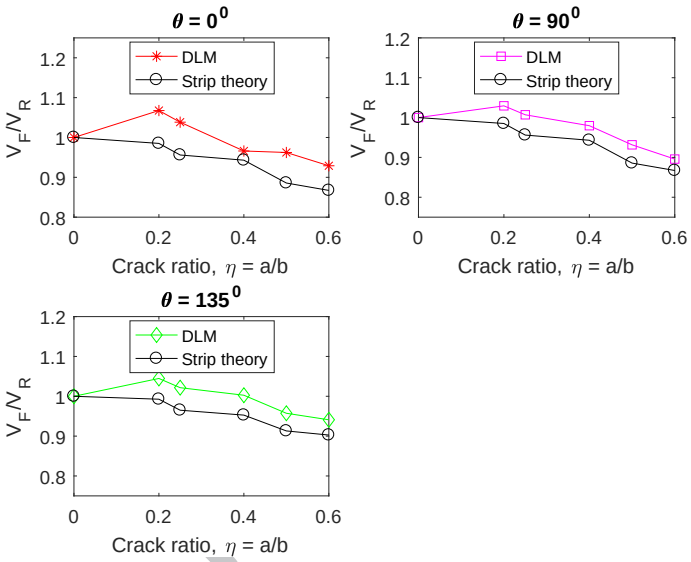

Figure 14: Comparison of DLM and Strip theory for normalized flutter speeds with respect to the crack ratio for case $\theta = 0^0$, $\theta = 90^0$ and $\theta = 135^0$

and the aerodynamic loads are estimated based on two-dimensional coefficients evaluated at the centre-line of the strip.

The comparison using both techniques is illustrated in Fig. 16. For this reason, the aerodynamics modelling accuracy using Strip theory is lower than DLM where the aerodynamic is consider strip by strip from the root to the tip of the composite plate, including the crack surface. The intention of computing the flutter speed based on Strip theory is to validate the work using DLM, which is not done by Wang et al [14]. Thus, it is believed that the aerodynamic modelling for the crack ratio of 0.2 is more reliable to be modelled with DLM.

To clarify this statement, the real and imaginary parts of the aerodynamic matrices for crack ratio = 0.2 are computed. Aerodynamic matrices of $\boldsymbol{Q}_{hh}$ in Eq. 32 shows the aerodynamic matrices computed for both real and imaginary parts where $h = 1$ and $h = 2$ are referred to the bending mode and torsion mode, respectively. In this case, Q_{11}, Q_{12}, Q_{21} and Q_{22} refer to the aerodynamic parameters for both real and imaginary parts in bending-bending, bending-torsion, torsion-bending and torsion-torsion, respectively.

$$\boldsymbol{Q}_{hh}(real\&imaginary) = \begin{bmatrix} Q_{11} & Q_{12} \\ Q_{21} & Q_{22} \end{bmatrix} \tag{32}$$

Both DLM and Strip theory computational aerodynamic matrices results are presented in Table 4.

Referring to Eq. 27, the real and imaginary parts of the aerodynamic matrices are contributed to the aerodynamics stiffness system and aerodynamic damping system, respectively. The negative sign value in Table 4 means the addition in the damping or stiffness system while the positive sign means the reduction to the damping of stiffness system. By analysing the data, the real part of the aerodynamic matrices using DLM is higher than the value computed using Strip theory. Thus, it means that the stiffness system estimated using DLM is less than strip theory.

The same analysing procedure is applied in evaluating the damping system. For this case, the imaginary values computed using DLM is less than the value estimated using strip theory. In this case, the lesser values of imaginary aerodynamic matrices have increased the damping system of DLM compared to Strip theory. For this case, the higher damping system has led to the stability of the cracked composite plate with the crack ratio of 0.2 to be increased; thus the flutter speed computed also has increased. This is the reason why the flutter speed of the composite plate with 0.2 is estimated to be higher using DLM compared to the flutter speed computed using strip theory.

6.4. Section b: Flutter effects on crack location

The objective of this subsection is to study the effects of the flutter speed when the location of the crack is changing from the root to the tip of the com-

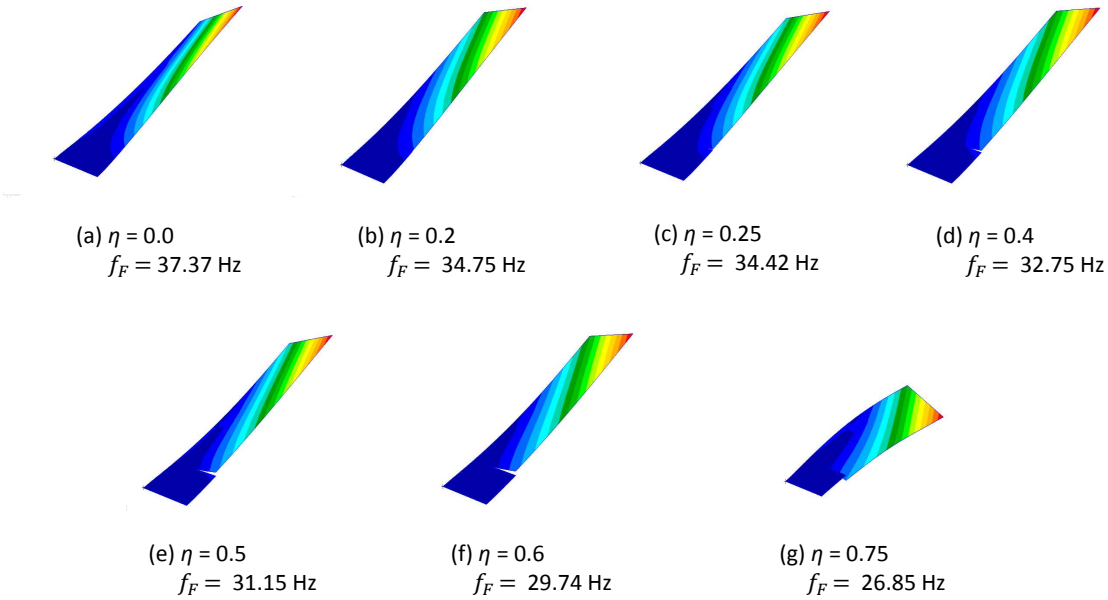

Figure 15: Flutter response modes for case $\theta = 0^0$ with variation of crack ratio

Table 4: Aerodynamic matrices data comparison between DLM and Strip theory for crack ratio 0.2

Aerodynamic parameter	Doublet Lattice Method	Strip Theory
Q_{11}	$2.47\text{x}10^1 - 8.68\text{x}10^2 i$	$-1.94\text{x}10^2 - 1.12\text{x}10^3 i$
Q_{12}	$-1.32\text{x}10^4 - 6.43\text{x}10^2 i$	$1.96\text{x}10^4 + 1.91\text{x}10^3 i$
Q_{21}	$8.58\text{x}10^1 + 8.13\text{x}10^2 i$	$2.22\text{x}10^2 + 8.99\text{x}10^2 i$
Q_{22}	$1.29\text{x}10^4 - 1.57\text{x}10^3 i$	$1.70\text{x}10^4 - 3.53\text{x}10^3 i$

posite plate. For this part; the crack length, $a = 0.02$ m is fixed for each case is validated with work done in [14]. Fig. 17 shows the results of normalized flutter speeds of V_F/V_R versus the crack location denoted as ξ_c for the unidirectional composites of 0^0, 90^0 and 135^0 orientations.

For the same analysed cases, the aerodynamics modelling for the specimens using DLM is repeated by changing it using Strip theory. The comparison results of normalized flutter speeds with respect to the crack location for case $\theta = 0^0$, $\theta = 90^0$ and $\theta = 135^0$ orientations using DLM and Strip theory ($\eta = 0.2$) are shown in Fig. 18.

In this case, V_F/V_R approximation using DLM seems to be higher than the estimation by using Strip theory. There is a significant part of this case where V_F/V_R at $\xi_c = 0.2$ is found to be slightly higher than V_F/V_R at $\xi_c = 0.4$. V_F/V_R are found to have increased after $\xi_c = 0.4$ till near the tip. Hence, the case of $\eta = 0.2$ is much complicated where the V_F/V_R is increased due to the crack ratio, as it is shown in the subsection 6.3.

Thus, to check the effect of the flutter speed when the location of the crack is changing from the root to the tip, the procedure is repeated using a different crack ratio which is $\eta = 0.6$. It stems from the fact of the consistency shows for the case $\eta = 0.6$ when the crack ratio is constructed in the subsection 6.3. V_F/V_R results for this case are shown in Fig. 19.

In Fig. 19, it turns out that the V_F/V_R plot shows consistency for all unidirectional composite plates of 0^0, 90^0 and 135^0 orientations. The result indicates that the V_F/V_R increases as the crack location moves from root to tip, as expected. This outcome is explained in Fig. 20. The flutter responses for unidirectional composite plate of $\theta = 0^0$ are plotted; the flutter frequency trend is found to have dropped as the crack location moves from root to tip. The reduction of flutter frequency allocates more time for the structure to swing, thus increase the flutter speed.

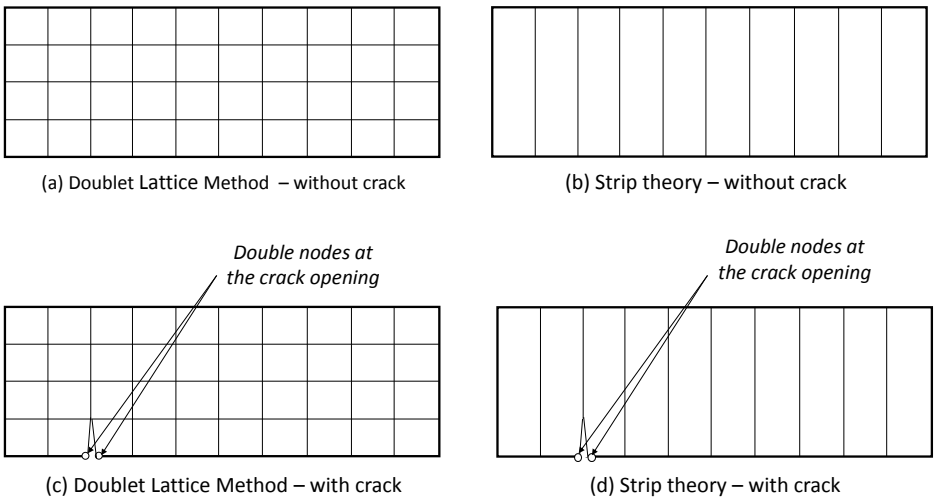

Figure 16: Comparison of aerodynamic modelling technique between Doublet Lattice Method and Strip theory for without crack and with crack specimen

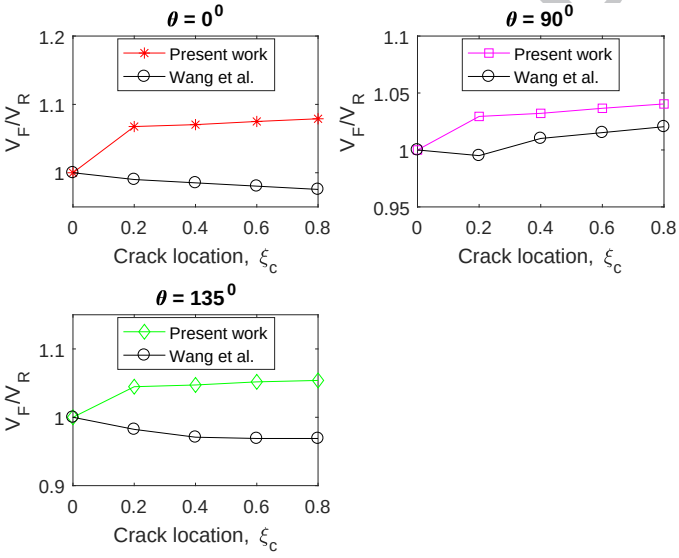

Figure 17: Normalized flutter speeds with respect to the crack location ($\eta = 0.2$) for case $\theta = 0^0$, $\theta = 90^0$ and $\theta = 135^0$

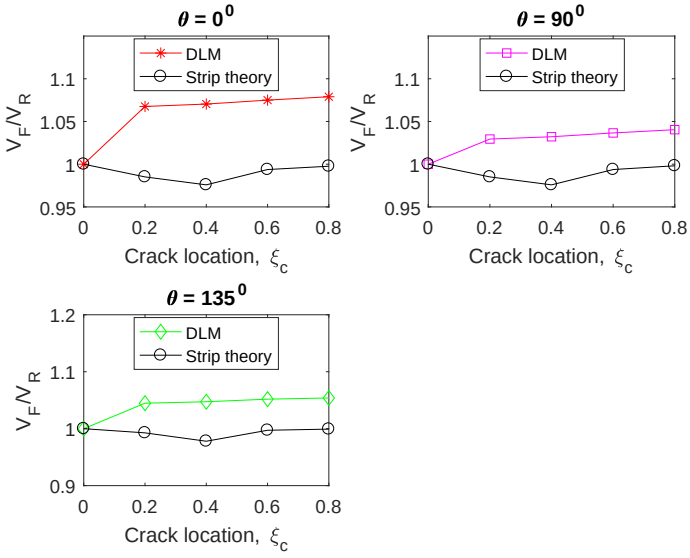

Figure 18: Comparison of DLM and Strip theory ($\eta = 0.2$) for normalized flutter speeds with respect to the crack location for case $\theta = 0^0$, $\theta = 90^0$ and $\theta = 135^0$

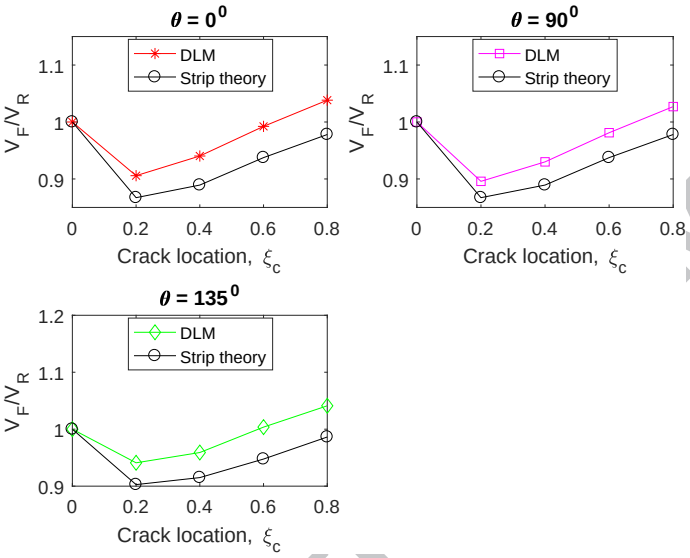

Figure 19: Comparison of DLM and Strip theory ($\eta = 0.6$) for normalized flutter speeds with respect to the crack location for case $\theta = 0^0$, $\theta = 90^0$ and $\theta = 135^0$

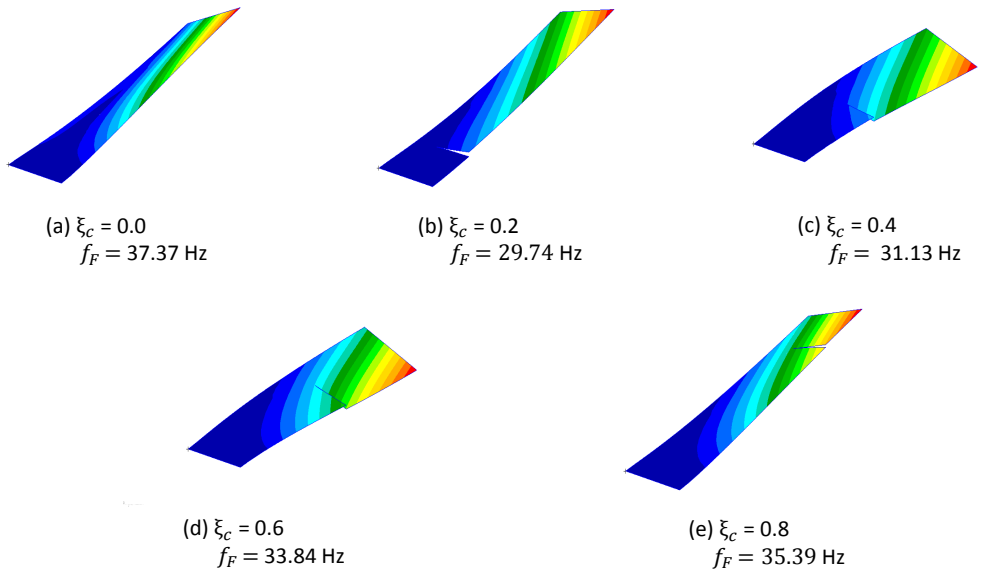

Figure 20: Flutter response modes for case $\theta = 0^0$ with variation of crack location

7. Conclusion

This paper offers a new investigation of the computational flutter estimation on a cracked composite plate. The study is divided into two sections; Section a: Flutter effects on the crack ratio and Section b: Flutter effects on crack location. To the authors' knowledge, this is the first time that the flutter on a cracked composite plate is assessed using the coupled FEM-DLM method. The variation of unidirectional angle led to different flutter speed obtained for each composite structures. Using FEM-DLM approach, the crack ratio initiated until 0.4 has increased the flutter speed for all unidirectional composite plates of 0^0, 90^0 and 135^0 orientations. The existence of crack on the structure results in a reduction of flutter speed from the crack ratio of 0.4 until the structure about to break.

The flutter analysis of fractured unidirectional composite plate due to the different crack location by fixing the crack length, η were performed. For this part, the analysis is performed where the crack location has been varied from the root to the tip of the plate. For $\eta = 0.2$, the normalized flutter speed V_F/V_R shows inconsistency since the effect of crack length is involved, where the existence of crack length, $\eta = 0.2$ has led to the flutter speed increment compared with the undamaged specimen. The investigation is repeated for $\eta = 0.6$ since the crack length shows a consistency in the crack length analysis. The results show that the normalized flutter speed for this crack length increases as the crack location moves from the root to the tip of the plate. The results of normalized flutter based on FE-DLM are compared with the results of normalized flutter based on FE-Strip. The comparison shows a very good agreement with a slightly higher of normalized flutter speeds estimation by FE-DLM compared to FE-Strip.

Acknowledgements

The authors gratefully acknowledge the financial supports from the Ministry of Education Malaysia and International Islamic University Malaysia. Special thanks to the National Space Agency Malaysia (ANGKASA) for their facilities and supports provided in conducting this research.

References

[1] Kushch VI, Sevostianov I, Mishnaevsky L. Effect of crack orientation statistics on effective stiffness of mircocracked solid. Int J Sol Struct 2009;46(6):1574 –88.

[2] Barbero EJ, Cortes DH. A mechanistic model for transverse damage initiation, evolution, and stiffness reduction in laminated composites. Compos Part B: Eng 2010;41(2):124 –32.

[3] Thompson WT. Vibration periods at tacoma narrows. Engineering News Record 1941;P477(1):61 –2.

[4] Billah KY, Scanlan RH. Resonance, tacoma narrows bridge failure. Amer J Physics 1991;59(2):118 –24.

[5] Castravete SC, Ibrahim RA. Effect of stiffness uncertainties on the flutter of a cantilever wing. AIAA J 2008;46(4):925 –35.

[6] NTSB . Aircraft accident brief - pilot/race 177, the galloping ghost, north american p-51d, n79111, reno, nevada, september 16, 2011. ntsb/aab-12/01. Tech. Rep. 2; National transportation Safety Board; 490 LEnfant Plaza, S.W. Washington, D.C. 20594; 2012.

[7] Birman V, Librescu L. Supersonic flutter of shear deformable laminated composite flat panels. J Sound Vibration 1990;139(2):265–75.

[8] Pidaparti RMV. Free vibration and flutter of damaged composite panels. Compos Struct 1997;38(1):477 –81.

[9] Pidaparti RMV, Chang CC. Finite element supersonic flutter analysis of skewed and cracked composite panels. Comput Struct 1998;69(2):265 –70.

[10] Natarajan S, Manickam G, Bordas S. Supersonic flutter analysis of functionally graded material plates with cracks. Frontiers Aero Eng 2013;2(2):91–7.

[11] Viola E, Marzani A, Fantuzzi N. Interaction effect of cracks on flutter and divergence instabilities of cracked beams under subtangential forces. Eng Fract Mech 2015;151:109 –29.

[12] Styuart AV, Livne E, Demasi L, Mor M. Flutter failure risk assessment for damage-tolerant composite aircraft structures. AIAA J 2011;49(3):655 –69.

[13] Georgiou G, Manan A, Cooper JE. Modeling composite wing aeroelastic behavior with uncertain damage severity and material properties. Mech Syst Signal Pr 2012;32:32 – 43.

[14] Wang K, Inman DJ, Farrar CR. Crack-induced changes in divergence and flutter of cantilevered composite panels. Struct Health Monit 2005;4(4):377–92.

[15] Kehoe M. A historical overview of flight flutter: Testing nasa technical memorandum 4720. Tech. Rep.; National Aeronautics and Space Administration; Edwards, California; 1995.

[16] FAA . Advisory circular (u. s. d. o. transportation, trans.: 23.629-1b - means of compliance with title 14 cfr, part 23, 23.629, flutter. Tech. Rep.; United States Department of Transportation; U.S.A; 2004.

[17] Nissim E, Gilyard GB. Method for experimental determination of flutter speed by parameter identification. Tech. Rep.; National Aeronautics and Space Administration; Ames Research Center Dryden Flight Research Facility Edwards, Calfornia; 1989.

[18] Perić D, SouzaNeto EAd, Carneiro Molina AJ, Partovi M. On Multiscale Analysis of Heterogeneous Composite Materials: Implementation of Micro-to-Macro Transitions in

the Finite Element Setting. Dordrecht: Springer Netherlands; 2007, p. 165 –85.
[19] Molina AJC, Curiel-Sosa JL. A multiscale finite element technique for nonlinear multi-phase materials. FE Anal Des 2015;94:64 – 80.
[20] Zhang C, Curiel-Sosa JL, Bui TQ. A novel interface constitutive model for prediction of stiffness and strength in 3d braided composites. Compos Struct 2017;163:32 – 43.
[21] Eshelby JD. The determination of the elastic field of an ellipsoidal inclusion, and related problems. Proc Math Phys Eng Sci 1957;241(1226):376–96.
[22] Voyiadjis GZ, Kattan PI. Mechanics of Composite Materials with MATLAB. Springer; 2005. ISBN 3540243534.
[23] Mori T, Tanaka K. Average stress in matrix and average elastic energy of materials with misfitting inclusions. Acta Metallurgica 1973;21(5):571 –4.
[24] Benveniste Y. A new approach to the application of mori-tanaka's theory in composite materials. Mech Mater 1987;6(2):147 –57.
[25] Albano E, Rodden WP. A doublet-lattice method for calculating lift distributions on oscillating surfaces in subsonic flows. AIAA J 1969;7(2):279–85.
[26] Abbas MK, Negm HM, Elshafei MA. Flutter and divergence characteristics of composite plate wing. Int J Eng Innov Technol 2014;4(2):105 –15.
[27] Curiel-Sosa JL, Gil AJ. Analysis of a continuum-based beam element in the framework of explicit-fem. FE Anal Des 2009;45(8):583 –91.
[28] Wright JR, Cooper JE. Introduction to Aircraft Aeroelasticity and Loads. 1 ed.; American Institute of Aeronautics Astronautics; 2007. ISBN 139781563479359.
[29] Corporation MSC. MSC.Nastran Version 68. In Aeroelastic Analysis Users Guide. M.S.C. Software Corporation; 2014.
[30] Nikpur K, Dimarogonas A. Local compliance of composite cracked bodies. Compos Sci Technol 1988;32(3):209 –23.
[31] Song O, Ha TW, Librescu L. Dynamics of anisotropic composite cantilevers weakened by multiple transverse open cracks. Eng Fract Mech 2003;70(1):105 –23.